PHYSICAL REVIEW A **68**, 042703 (2003)

Excited-state evolution probed by convoy-electron emission in relativistic heavy-ion collisions

Y. Takabayashi,[1] T. Ito,[1] T. Azuma,[2] K. Komaki,[1] Y. Yamazaki,[1,3] H. Tawara,[4] E. Takada,[5] T. Murakami,[5]
M. Seliger,[6] K. Tőkési,[7] C. O. Reinhold,[8] and J. Burgdörfer[6]
[1]*Institute of Physics, Graduate School of Arts and Sciences, University of Tokyo, 3-8-1 Komaba, Meguro, Tokyo 153-8902, Japan*
[2]*Department of Physics, Tokyo Metropolitan University, Hachioji, Tokyo 192-0397, Japan*
[3]*Atomic Physics Laboratory, RIKEN, Wako, Saitama 351-0198, Japan*
[4]*National Institute for Fusion Science, Toki, Gifu 509-5292, Japan*
[5]*National Institute of Radiological Sciences, Inage, Chiba 263-8555, Japan*
[6]*Institute for Theoretical Physics, Vienna University of Technology, A-1040 Vienna, Austria*
[7]*Institute of Nuclear Research of the Hungarian Academy of Sciences, (ATOMKI), P.O. Box 51, H-4001 Debrecen, Hungary*
[8]*Physics Division, Oak Ridge National Laboratory, Oak Ridge, Tennessee 37831-6372, USA*

(Received 25 April 2003; published 8 October 2003)

We present a joint experimental and theoretical study of convoy-electron emission resulting from highly-charged-ion transport through carbon foils at moderately relativistic speeds. Energy spectra of electrons ejected at 0° have been measured for 390 MeV/u hydrogen-like Ar^{17+} ions and 460 MeV/u ($\beta = v/c = 0.74, \gamma = 1.49$) Fe^{25+} $(1s)$, Fe^{24+} $(1s^2)$, and Fe^{23+} $(1s^2 2s)$ incident on carbon foils with thicknesses from 25 to 8700 $\mu\mathrm{g/cm}^2$. Due to this unprecedented wide range of thicknesses, the sequential excitation and ionization of initially deeply bound electrons to highly excited states and continuum states can be followed in considerable detail. The analysis of the spectra is aided by simulations based on the classical transport theory which has been extended to relativistic energies and to multielectron projectiles. The motion of the projectile electron inside the solid target is calculated taking into account the Coulomb potential of the projectile ion and the multiple stochastic collisions with target cores and target electrons. Different phases of the convoy-electron emissions can be disentangled: direct ejection to the continuum, the transient buildup of an excited-state wave packet followed by ionization, and postionization modification of the continuum spectrum. We find good agreement between experiment and simulation for the evolution of charge states and the emission spectrum.

DOI: 10.1103/PhysRevA.68.042703 PACS number(s): 34.50.Fa, 34.10.+x

I. INTRODUCTION

The angular and energy distributions of electrons emitted in ion-atom and ion-solid collisions have been studied extensively during the last few decades in the regime of nonrelativistic projectile velocities [1,2]. One of the most prominent features of these emission spectra is that in the forward direction they exhibit a cusp-shaped peak at the energy corresponding to the same velocity as the incident ion. This peak is referred to as convoy-electron peak (CEP). Mainly two processes are responsible for this electron emission: the electron loss to the continuum (ELC) originating in a direct transition from the initial state of the projectile electron to the low-lying continuum of the ion [3] and the capture of a target electron to the low-lying continuum of the projectile (ECC) [4–6]. At intermediate projectile velocities both processes significantly contribute to the CEP, posing complications when extracting detailed information about each emission mechanism separately. Moreover, in ion-solid collisions, a large array of multiple-scattering processes in the solid contributes. Relating the emitted electron spectrum to the microscopic scattering processes that generate them is therefore exceedingly difficult. Convoy-electron emission is one signature of the evolution of an electronic state of the projectile traversing a solid. The latter problem continues to attract considerable interest, among other reasons, because of its relevance for the injection problem of high current spallation neutron sources [7] and for x-ray emission [8,9].

The convoy-electron spectra for ion-solid collisions have been frequently analyzed by comparing them with the ECC and ELC electron spectra for ion-atom collisions. For the ECC process, the electron spectrum was reported to be skewed toward lower energy [1]. On the other hand, for the ELC process, the shape of the electron spectrum is forward-backward symmetric. In the projectile frame, the ELC electrons tend to be emitted transversely, i.e., perpendicular to the beam direction, which leads to the narrow cusp peak in the laboratory frame [10,11]. Berry *et al.* measured the angular distribution of convoy electrons in ion-solid collisions [12]. The observed angular distribution of convoy electrons resembled that of ELC electrons except that the former is more strongly transverse. For convoy-electron distributions of 36 MeV/u Ar^{9+} ion collisions with thin carbon foils, Gibbons *et al.* [13] found rapidly changing anisotropy parameters as a function of the target thickness which were attributed to electron emission inside the solid from high-n states of the projectile.

All experiments on convoy-electrons to date have been performed in the MeV/u energy region. In this energy range, it is difficult to fulfill single collision conditions because the average distances between two collisions [the mean free paths (MFP's)] for capture, excitation, and scattering of free electrons are short in comparison to the experimentally available and reliably controllable foil thicknesses. Therefore, a detailed study of the evolution of convoy-electron spectra from the near-single collision regime to the thick-foil multiple-scattering regime has been missing. In order to follow this evolution in detail and to disentangle microscopic

©2003 The American Physical Society

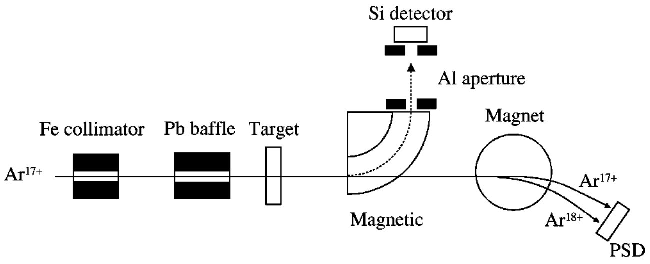

FIG. 1. Schematic drawing of the experimental setup. Trajectories for Ar ions are also shown.

processes governing the emission and modification of the convoy spectrum we have employed much higher, moderately relativistic, energy Ar^{17+} ions of 390 MeV/u ($\beta = v_P/c = 0.71, \gamma = 1.42$) and carbon foils with thicknesses d from 25 to 8700 μg/cm^2 [14]. For amorphous carbon a thickness of 1 μg/cm^2 corresponds to 100 a.u. or to the 20-fold of the atomic mean nearest-neighbor spacing. The thickness d is also a direct measure for the elapsed time, in the frame of the projectile $t \approx d/(v_P \gamma)$ (v_P: ion velocity), for the evolution of the wave packet of the projectile electron inside the solid. We will use thickness and time interchangeably to parametrize the evolution of the initial projectile state. This wide range of thicknesses provides the opportunity to follow the electronic evolution for a single active electron from its initial ground state to its final state in the continuum subject to up to hundreds of collisions. In this energy range:

(i) The electron capture process is completely negligible compared to the ionization process. Accordingly, contributions from target electrons to convoy-electron emission can be safely neglected. Consequently, only the electrons carried into the collisions by the projectile are active participants and they provide the exclusive source for the observed electron spectra. An effective one-active electron picture is therefore applicable.

(ii) All relevant MFP's are long at this energy. For example, the MFP for projectile $1s$ ionization in carbon is estimated to be 3000 μg/cm^2 [15]. Even the shortest MFP in the system, the MFP for free-electron scattering, is ≈ 30 μg/cm^2 [16] and thus larger than the thickness of the thinnest foil used. Moreover, dependences on the initial state of the electron to be ionized can be investigated by employing different projectiles. We have therefore also measured the spectra of convoy-electrons produced by 460 MeV/u ($\beta = v_P/c = 0.74, \gamma = 1.49$) hydrogenic $\mathrm{Fe}^{25+}(1s)$, helium-like $\mathrm{Fe}^{24+}(1s^2)$, and lithium-like $\mathrm{Fe}^{23+}(1s^2 2s)$ incident on carbon foils with thicknesses ranging from 50 to 1900 μg/cm^2.

In this paper, our experimental findings are compared with results of calculations performed with the recently developed classical transport theory (CTT) [16–18]. Within this framework the electronic motion is determined by the projectile Coulomb potential and the stochastic forces due to multiple scattering with target electrons and target cores. Application of the CTT to the present experimental conditions for highly charged ions requires the extension to the treatment of deeply bound electrons where quantum effects may play an important role [19,20]. Moreover, the analysis of the Fe data requires the extension of the one-electron transport theory to multielectron projectiles, which can be performed within the framework of the independent-particle approximation (IPA) [21].

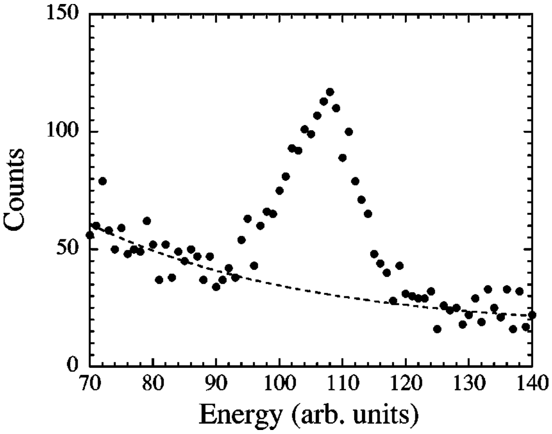

FIG. 2. Typical pulse-height distribution measured with the SSD. The dashed line shows the fit to the background.

The plan of this paper is as follows. In Sec. II we briefly describe the experimental setup. In Sec. III we discuss the modifications and extensions of the classical transport theory as required to describe the current range of projectile charges. Detailed comparisons between experiment and theory are given in Sec. IV, followed by a short summary in Sec. V. Atomic units are used unless otherwise stated.

II. EXPERIMENT

Figure 1 displays the experimental setup schematically. Beams of 390 MeV/u Ar^{17+} and 460 MeV/u Fe^{q+} ($q = 23,24,25$) ions were provided by the Heavy Ion Medical Accelerator in Chiba (HIMAC). A 50-mm thick Fe collimator with an inner diameter of 1 mm was located 6.5 m upstream from a carbon foil target. In the case that the size of the beam spot was small enough, the collimator was removed. Although the beams of Ar and Fe ions are stopped in the collimator, the light particles produced via nuclear reaction in collisions of the beam with the collimator escape from it. In order to eliminate such fragments, a 150-mm thick Pb baffle with an inner diameter of 10 mm was placed 0.35 m upstream from the target. We prepared carbon foils with thicknesses from 25 to 8700 μg/cm^2 as targets. The diameter of the beam was about 2 mm at the target.

The energy of the detected convoy-electrons is around 200 keV. An electrostatic electron analyzer is not suited for measuring the spectra of such high-energy electrons. In order to obtain the spectra of the electrons ejected at 0°, we adopted a magnetic analyzer with a 105 mm central orbit radius and a 90° deflection angle. A silicon surface-barrier detector (SSD) with a depletion layer of 5 mm was used as an electron detector. By scanning the strength of the magnetic field, we obtained the momentum spectra and transformed them to the energy spectra. Figure 2 shows the pulse-height distribution measured with the SSD with the fit for background subtraction. The use of the SSD is essential to discriminate against the background signal such as electrons from other sources and γ rays. Two 5-mm thick Al apertures with an inner diameter of 5 mm were placed at the exit of the magnet and also in front of the electron detector. These apertures determine the momentum resolution ($\Delta p/p \sim 0.02$) and the acceptance angle ($\Delta\theta \sim 1°$). The stopping power for 214 keV electrons, isotachic to 390 MeV/u Ar ions, in carbon is 2.4 eV/(μg/cm^2) [22] and, therefore, the energy loss is completely negligible for a thin target (e.g., 25 μg/cm^2 carbon foil). The absolute electron energy was thus calibrated assuming that the peak energy of convoy-electrons for Ar^{17+} and Fe^{25+} ions incident on a thin target is equal to that of an electron with the same velocity as the incident ion. During the measurement, the beam intensity was more than 10^4 particles per second (pps). We placed a Cu foil of 50 μm thickness at the end of the beam line, and monitored the beam intensity by measuring Cu K x-rays emitted in collisions of the projectile ions with the Cu foil using a Si(Li) detector.

We also measured the charge-state distributions of the ions transmitted through the carbon foils. The ions were charge separated by a magnet with a field strength of 0.5 T located 1.3 m downstream from the target and detected with a two-dimensional (2D) position-sensitive Si detector (PSD) located 5.6 m downstream from the targets. In this measurement, the beam intensity was reduced to $\sim 10^3$ pps to avoid pileup.

For thicker targets ($\geqslant 1000$ μg/cm^2), we evaluated their thicknesses by measuring the energy loss. A beam of 6 MeV/u protons was supplied from the tandem accelerator at the University of Tsukuba. The energy of the proton transmitted through the carbon foil was measured with a SSD of 500 μm in thickness. The observed width of the energy-loss peak was broader than the energy resolution of the SSD and the energy straggling of the proton. Taking into account the widths originating from these contributions, the inhomogeneity of the target thickness was extracted from the width [full width at half maximum (FWHM)] of the proton energy-loss peak. For thinner targets ($\leqslant 1000$ μg/cm^2), we adopted the values for the thickness estimated by a carbon foil supplier with an accuracy and inhomogeneity of ±10% [23].

III. THEORY

The evolution of the state of the electron is represented within the classical transport theory (CTT) [16–18] by a probability density in phase space $\rho_{cl}(\vec{r},\vec{p})$ which is initially given by a microcanonical ensemble with the binding energy of the active electron in the ground state. For hydrogenic 1s states, the momentum distribution $\rho_{cl}(p)$ agrees with its quantum counterpart. The time evolution of the electron is then given by a reduced Liouville equation which is solved by test particle discretization (i.e., classical trajectory Monte Carlo sampling). Microscopically, the dynamics of each test particle is governed by a Langevin equation involving both a deterministic Coulomb force and a stochastic force acting on the electron:

$$\dot{\vec{p}} = -\vec{\nabla} V_P(\vec{r}) + \sum_i \Delta\vec{p}_i \delta(t-t_i), \tag{1}$$

where V_P denotes the interaction potential between the active electron and the projectile. Here and in the following, $(\vec{r},\vec{p})$ denote the position and the momentum of the electron in the projectile frame whereas primed variables $(\vec{r}\,',\vec{p}\,')$ correspond to the target frame. For hydrogenic ions, $V_P(\vec{r}) = -Z_P/r$, with the projectile charge Z_P. For multielectron projectiles V_P represents the effective potential taking into account partial screening effects by passive projectile electrons. The high projectile velocity allows one to neglect modifications of V_P by dynamical screening of the projectile by target electrons inside the solid [24]. The effective screening length for dynamical screening $l'_{sc} = v_P/\omega_P \approx 100$ a.u. (ω_P: plasma frequency of the medium) in the restframe of the target and the corresponding screening length in the projectile frame $l_{sc} = l'_{sc}/\gamma$ is large compared to the size of (even highly excited) projectile states. At high velocities, the electron-solid interaction can be treated in the impulsive momentum-transfer approximation, i.e., momenta $\Delta\vec{p}_i$ are transferred instantaneously at collision times t_i, reducing the transport problem to a random walk of the projectile electron along Kepler orbits subject to a stochastic sequence of momentum transfers. The probability distributions of $\Delta\vec{p}_i$ and t_i are microscopically determined [17] within linear-response theory, i.e., Eq. (1) does not contain any adjustable parameter. The $\Delta\vec{p}_i$ distribution follows from the relativistic differential inverse mean free path, whereas the flight times $\Delta t_i = t_i - t_{i-1}$ between two collisions are obtained from the corresponding integral inverse mean free path. Outside the solid the time evolution of the electron associated with the projectile is determined by the Coulomb force represented by the first term in Eq. (1) only. In a classical picture the unperturbed electronic motion is described by Kepler orbits at constant energies [17].

Essential inputs for the treatment of the random walk of the electron (bound and in continuum) as described by the Langevin equation (1) are the differential and integral inverse mean free paths for the interactions with the solid. The collisional interactions determining $\Delta\vec{p}_i$ and Δt_i are the scattering of the electron at the screened heavy nuclei in the solid on one hand and interactions with the fermionic N-body system of target electrons on the other hand.

We briefly review the calculation of the differential inverse mean free paths (DIMFP's) used as input for the Langevin equation (1). More details can be found in Refs. [16,17,25]. Different scattering processes involving the projectile electron are considered: (a) scattering at the screened core of target atoms and (b) scattering at a quasifree electron gas of the valence electrons leading to longitudinal and transverse excitations.

The screened Coulomb potential of the target cores is described by $V(r') = -(Z_T/r')e^{-r'/a}$ where $a = 0.885 Z_T^{-1/3}$ is the Thomas-Fermi screening radius and Z_T the target nuclear charge [26]. Since the projectile electron is much lighter than the target atom it scatters at, practically no energy is transferred to the projectile. Therefore we will refer to scattering at atomic cores as elastic interaction hereafter. We point out that elastic collisions in the rest frame of the target, nevertheless, result in excitation of the projectile electronic state. The doubly differential inverse mean free path (DIMFP) as a function of differential energy and momentum transfer, $d\omega$ and dq, is given in first-order Born approximation by [17,27]

$$\frac{d^2\lambda_1^{-1}}{d\omega dq}=\frac{8\pi Z_T^2 N}{v_e'^2}\frac{\delta(\omega)}{q^3[1+(qa)^{-2}]^2}, \tag{2}$$

with the atomic number density $N\simeq 9.9\times 10^{22}/\mathrm{cm}^3$ for amorphous carbon corresponding to a density of $\rho=2\ \mathrm{g/cm}^3$. The delta function $\delta(\omega)$ corresponds to zero energy transfer to the projectile electron and v_e' is the electron velocity. More accurate elastic-scattering potentials can be treated within the partial-waves method [28]. We choose Eq. (2) in favor of a faster evaluation within the Monte Carlo simulation in order to decrease the statistical error which dominates over the error introduced by the simplified potential.

The interaction with the target electron gas leads to the creation of a plasmon or particle-hole pairs. The high projectile velocity allows us to treat the problem in linear-response theory. The electrostatic Coulomb interaction between the projectile electron at position $\vec{r}\,'$ with a target electron at position $\vec{r}_j\,'$ can be expressed as a Fourier integral over the momentum transfer $\vec{q}=\vec{p}_i-\vec{p}_f$ written as a tensor product acting in the projectiles subspace $\langle \vec{p}_f\,'|V_l(\vec{q})|\vec{p}_i\,'\rangle$ and in the targets $\langle n|V_l(\vec{q})|0\rangle$ subspace as $V_l(\vec{q})=q^{-2}e^{-i\vec{q}\cdot\vec{r}\,'}\otimes\Sigma_j e^{i\vec{q}\cdot\vec{r}_j\,'}$. This interaction exerts a force parallel to $\vec{q}$ and is accordingly called "longitudinal" hereafter. In first Born approximation the probability for exciting a target atom from the ground state to an excited state of energy E_n while transferring momentum $\vec{q}$ and energy ω to the projectile electron per unit pathlength is given by the DIMFP as [29]

$$\frac{d^2\lambda_2^{-1}}{d\omega dq}=\frac{2}{\pi v_e'^2 q}\ \mathrm{Im}\left[\frac{-1}{\varepsilon(q,\omega)}\right], \tag{3}$$

where $\varepsilon^{-1}(q,\omega)$ is the inverse dielectric function of the electron gas.

At relativistic energies a second inelastic interaction mechanism with target electrons is the emission and reabsorption of virtual photons with momenta $\pm\vec{q}$ exciting intermediate target states with energies $cq\pm E_n$. The interaction term for the projectile emitting a photon with momentum $\vec{q}$ is given by $-c\vec{\alpha}\cdot\hat{A}_s e^{-i\vec{q}\cdot\vec{r}}$ with the Dirac current operator $-c\vec{\alpha}$ and the unit polarization vector $\hat{A}_s$ with the two orthogonal polarizations $s=1,2$ [29]. The probability amplitude for absorbing this photon by the target is proportional to the matrix elements of the operator $-c\vec{\alpha}\cdot\hat{A}_s e^{-i\vec{q}\cdot\vec{r}_j}$. Since this force is orthogonal to the propagation direction of the emitted/absorbed photon, we refer to this interaction as the "transverse" excitation. As for the longitudinal excitations (3), the DIMFP for transverse excitation can be expressed in terms of the complex dielectric response function $\varepsilon(q,\omega)=\varepsilon_1(q,\omega)+i\varepsilon_2(q,\omega)$ as

$$\frac{d^2\lambda_3^{-1}}{d\omega dq}=\frac{2\beta'^2}{\pi c^2 q}\frac{\varepsilon_2\sin^2\Psi\cos^2\Psi}{(1-\beta'^2\varepsilon_1\cos^2\Psi)^2+\beta'^4\varepsilon_2^2\cos^4\Psi}, \tag{4}$$

where $\beta'=v_e'/c$ and Ψ is the angle between the incident momentum $\vec{p}_i\,'$ and the momentum transfer $\vec{q}$.

The key ingredient for the description of both longitudinal and transverse projectile-target electrons interaction is the inverse dielectric response function $\varepsilon^{-1}(q,\omega)$. In the present approach $\varepsilon^{-1}(q,\omega)$ is parametrized in terms of a sum of n Drude-type functions introduced by Ashley [30]. The parameters are determined from the optical limit $(q=0)$ where experimental optical data for the loss function $\mathrm{Im}[-1/\varepsilon(q=0,\omega)]$ are available for many materials. For carbon the loss function can be fitted by a sum of five Drude-type functions [31,30]

$$\mathrm{Im}\left[\frac{-1}{\varepsilon(q,\omega)}\right]=\sum_{j=1}^{n}\frac{\omega_{pj}^2\eta_j\omega}{(\omega_{0j}^2(q)-\omega^2)^2+\eta_j^2\omega^2}, \tag{5}$$

fixing the parameters ω_{pj}, ω_{0j} for η_j $(j=1,\ldots,5)$ in Eq. (5) for $q=0$. The use of a relativistic free particle dispersion relation for the resonance frequency $\omega_{0j}(q)=\omega_{0j}+c^2(\sqrt{1+q^2/c^2}-1)$ allows one to access regions with $q\neq 0$.

We discuss in the following briefly the extension of the CTT required for the present application of sequential ionization of deeply bound electrons. A recently developed quantum trajectory Monte Carlo method (QTMC) [20,24] reduces to the CTT when the electron-solid interaction is treated as quasifree electron scattering and the classical limit is taken. For deeply bound electrons, the quasifree electron approximation is poorly justified. Because the continuum emission spectrum is difficult to treat within the QTMC we employ the CTT instead, taking into account, however, the suppression of small momentum transfers in soft collisions for deeply bound electrons. In a quantum-mechanical treatment of the projectile electronic system, the final state after a collision is restricted by the discrete level structure of bound states. A classical description of the transport problem does not contain such a feature. To partly account for this inadequacy we introduce the requirement of a minimum energy transfer ω_{min} in the rest frame of the projectile ion, which is determined by the energy gap between the binding energy before (E_{n_i}) and after (E_{n_f}) collision as $\omega_{min}=E_{n_f}-E_{n_i}=E_{n_i}[n_i^2/n_f^2-1]$. For excitation to the next higher energy level $(n_f=n_i+1)$, the expression simplifies to $\omega_{min}=E_{n_i}[(1+1/n_i)^{-2}-1]$. Within a classical simulation the principal action (quantum number n) is a positive real number given by $n=Z_P/\sqrt{-2E_e}$ where E_e is the binding energy of the electron in the rest frame of the projectile ion. Accordingly, we introduce a minimum momentum transfer q_{min} as a function of binding energy E_e, which is given by

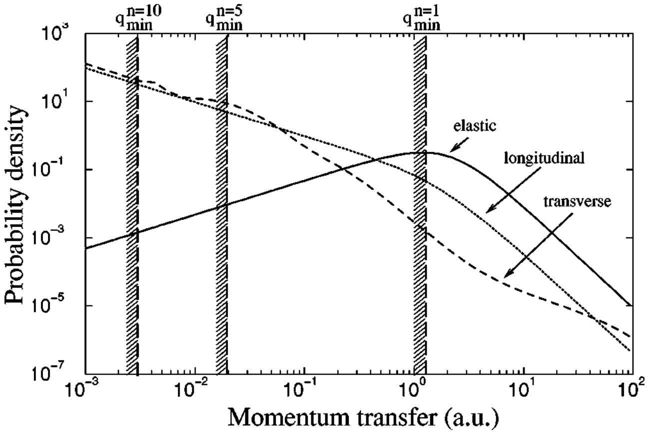

FIG. 3. Momentum-transfer distributions for elastic (solid line), inelastic longitudinal (dotted line), and inelastic transverse (dashed line) collisions evaluated at the initial projectile velocity of 97 a.u. with cutoff for the minimum momentum transfer for excitation of the ground state ($n=1$) and of excited states $n=5$ and $n=10$ indicated by vertical lines.

$$q_{min}=\frac{\omega_{min}}{v_e'}=\frac{E_e}{v_e'}[(1+\sqrt{-2E_e}/Z_P)^{-2}-1]. \tag{6}$$

Equation (6) defines a lower cutoff for the momentum transfered by the collision in the modified differential inverse mean free path,

$$\left(\frac{d^2\lambda_i^{-1}}{d\omega dq}\right)_m=\frac{d^2\lambda_i^{-1}}{d\omega dq}\,\theta(q-q_{min}), \tag{7}$$

through the Heaviside step function $\theta(q-q_{min})$. In Eq. (7) $d^2\lambda_i^{-1}/d\omega dq$ is the original DIMFP for free electrons in first Born approximation differential in energy transfer $d\omega$ and momentum transfer dq for electron-target core scattering ($i=1$) and electron-electron scattering ($i=2,3$). In the limit of states with small binding energy $E_e\rightarrow 0$, q_{min} tends to zerolike $q_{min}\rightarrow-(E_e/v_e')\sqrt{-8E_e}/Z_P$. Consequently, the modified DIMFP, $[(d^2\lambda_i^{-1})/d\omega dq]_m$ in Eq. (7), resembles the free-electron DIMFP in this limit. We thus partly include the quantum-mechanical suppression of small momentum transfers in our classical treatment of collisions of bound electrons.

Figure 3 illustrates the effect in the cutoff for the DIMFP for both core scattering and relativistic longitudinal and transverse contributions to the e-e scattering (for details of the relativistic MFP calculation see Ref. [25]) for different principal quantum numbers n (i.e., different binding energies). The relative importance of the cutoff is largest for electron-electron scattering while for core scattering the effect is less dramatic because the mean momentum transfer is larger. In the early stages of the excitation ladder when the electron is still close to the ground state, the cutoff leads to a clear dominance of core scattering contributions in the stochastic perturbation [Eq. (1)]. In the later stages when the electron has been already lifted into higher excited states the cutoff for small values of q tends to zero and e-e collisions are no longer suppressed by the requirement $q>q_{min}$. The latter start to significantly contribute to the interaction with the solid by perturbing the highly excited states while the large momentum transferred by core collisions tends to immediately ionize the electron. Finally, for transport of free electrons all values of q are allowed ($q_{min}=0$). In this region energy straggling is primarily caused by e-e scattering while the electrons are removed from the small-angle forward cone by deflection in elastic collisions. In our Monte Carlo simulation we have the opportunity to follow the time evolution of the electrons from the deeply bound ground state to highly excited states and then finally into the continuum. Their signatures in the spectra of emitted electrons will be discussed in detail in the following section.

A second modification concerns the treatment of multielectron projectiles. In the presence of additional electrons bound to the projectile, the interaction potential of the active electron k with the constituents of the projectile becomes

$$V_P(\vec{r}_k,t)=-\frac{Z_P}{r_k(t)}+\sum_{j\neq k}\frac{1}{|\vec{r}_k(t)-\vec{r}_j(t)|}, \tag{8}$$

consisting of the Coulomb interaction with the bare nucleus (1st term) and a sum of the Coulomb interactions with the other projectile electrons (2nd term). Solving Eq. (1) with the potential [Eq. (8)] represents a formidable task since every projectile electron is subject to transport and thus performs a coupled random walk in phase space during the time evolution. To further complicate matters, a classical many-electron atom is highly unstable due to spontaneous autoionization. We therefore simplify the problem by invoking the independent-particle approximation (IPA) [21]. Accordingly, we employ a state-dependent yet time-independent mean-field potential $V_P^{(nl)}$ for a given electron which accounts for partial screening. The construction of $V_P^{(nl)}$ makes use of the fact that for that high projectile velocities and a strong suppression of capture, multielectron ionization in a multiple-scattering environment is sequential with the more weakly bound electrons emitted first. This feature allows us to introduce the initial binding energy of each electron as an order parameter, $E_k<E_{k+1}$, where E_k is given by the sequential ionization potential of the kth electron. The potential of Eq. (8) can be simplified within the IPA by including in $V_P^{(nl)}(\vec{r}_k)$ only the sum over more deeply bound electrons ($j<k$) [i.e., assuming that during the excitation process of the kth electron the more deeply bound electrons ($j<k$) remain in the ground state]. Consequently, for the electron k in the state nl the potential takes the form

$$V_P^{(nl)}(\vec{r}_k)=-\frac{Z_P}{r_k}+\sum_{j<k}\left\langle\Psi_j(\vec{r}_j,Z_P^{(k)})\left|\frac{1}{|\vec{r}_k-\vec{r}_j|}\right|\Psi_j(\vec{r}_j,Z_P^{(k)})\right\rangle. \tag{9}$$

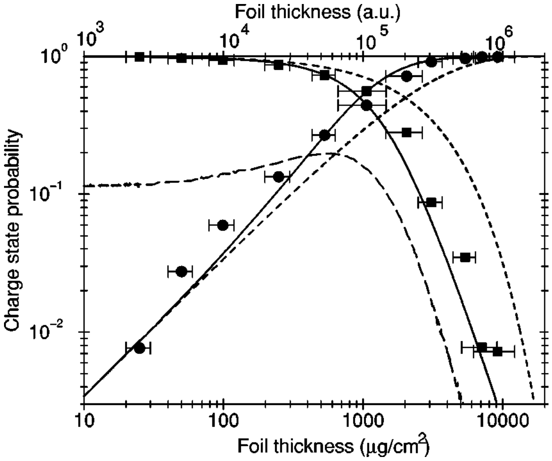

FIG. 4. Outgoing fractions of Ar^{17+} and Ar^{18+} ions as a function of foil thickness resulting from the transmission of 390 MeV/u Ar^{17+} ions through amorphous carbon foils. Experimental data for Ar^{17+} (squares) and Ar^{18+} (circles); short dashed line, simulation neglecting multiple excitation (i.e., direct ionization from ground state); solid line, full CTT simulation; and long-dashed line, electron emission probability per 10^6 a.u. path length.

For $k=1$ the potential $V_P^{(nl)}(\vec{r}_1)$ reduces to the state-independent bare Coulomb potential of the unscreened projectile nucleus. The experimental studies [14] have been performed with iron projectiles carrying up to three electrons into the collision. The explicit form of $V_P^{(nl)}(\vec{r}_k)$ for $(k=2,nl=1s)$ and $(k=3,nl=2s)$ is obtained using the radial hydrogenic wave function

$$\Psi_j(\vec{r}_j,Z_P^{(k)})=e^{-Z_P^{(k)}r_j}\sqrt{Z_P^{(k)3}/\pi} \tag{10}$$

of the $(1s)$ ground state in Eq. (9) with the effective nuclear charge of $Z_P^{(k)}$ which accounts for the screening by $k-2$ electrons. Accordingly, for $k=2, Z_P^{(2)}=Z_P$. For $k=3$, $Z_P^{(3)}$ is found for the He-like core by minimizing the ground-state energy to be $Z_P^{(k)}=Z_P-5/16$ [32]. The charge $\sigma=5/16$ represents the screening effect felt by each electron during its motion in the Coulomb field of the nucleus due to the presence of the other electron in the $1s$ ground state. This simple screened hydrogenic eigenfunction causes a decreasing error with increasing Z_P resulting from the fact that the interaction of each electron with the nucleus increases as Z_P^2 while the electron interaction energy increases only linearly with Z_P. Because in this work we consider a large $Z_P=26$, the use of such a simple approximation appears justified.

Performing the integration in Eq. (9) gives a screening potential

$$V_P^{(nl)}(r_k)=-\frac{Z_P-(k-1)}{r_k}-(k-1)\left(Z_P^{(k)}+\frac{1}{r_k}\right)e^{-2Z_P^{(k)}r_k}, \tag{11}$$

which properly interpolates between the limits $-Z_P/r$ for $r\to 0$ and $[Z_P-(k-1)]/r$ for $r\to\infty$. With this choice for the potential, the time evolution of each projectile electron is independent from the state of the other projectile electrons. Therefore, we can follow the time evolution of each projectile electron as a random walk in phase space in separate CTMC runs. Furthermore, the charge state of the projectile can be determined by binomial statistics with probabilities determined by the CTT probabilities for each electron. Let $a_k(d)$ be the probability for finding the kth electron in the continuum at the propagation distance d and $b_k(d)=1-a_k(d)$. The resulting charge-state fraction $P_{q\to q'}(d)$ of the iron projectile Fe^{q+} during the transport can be determined from these independent electron emission probabilities $a_k(d)$. For example, for incident Li-like Fe^{23+} we have

$$P_{23\to 23}(d)=\prod_{k=1}^{3} b_k(d), \tag{12a}$$

$$P_{23\to 24}(d)=\sum_{k\neq j\neq l=1}^{3} a_k(d)b_j(d)b_l(d), \tag{12b}$$

$$P_{23\to 25}(d)=\sum_{k\neq j\neq l=1}^{3} a_k(d)a_j(d)b_l(d), \tag{12c}$$

$$P_{23\to 26}(d)=\prod_{k=1}^{3} a_k(d), \tag{12d}$$

and analogous expressions for other incident charge states.

IV. RESULTS AND DISCUSSION

A. Thickness dependence of convoy-electrons produced by 390 MeV/u Ar^{17+} ions

Figure 4 shows the charge-state distribution as a function of carbon foil thickness for 390 MeV/u incident Ar^{17+} ions. Since at very high collision energies the electron-capture process is negligible, only Ar^{17+} and Ar^{18+} ions were observed. The fraction of Ar^{18+} ions was 0.8% at 25 μg/cm^2, and increased to more than 99% at $\sim$10000 μg/cm^2. The charge-state distribution is still not fully equilibrated even at $\sim$10 000 μg/cm^2. The agreement with the simulation based on the CTT is excellent over orders of magnitude in thickness and probability. We also show the calculated charge-state probabilities when only direct ionization from ground state is taken into account, i.e., when stepwise excitation in multiple collisions prior to ionization is neglected. The charge-state probability $P_{17}(d)$ for the initial state (Ar^{17+}) obeys in this case the simple exponential decay law $P_{17}(d)=\exp(-d/\lambda_{1s})$ with the MFP for ionization from the $1s$ ground state $\lambda_{1s}\simeq 3000$ μg/cm^2. The fact that we observe clear deviations from such a simple exponential decay provides direct evidence for the random walk in state space prior to ionization. The probability per atomic unit path length for emitting an electron is proportional to the slope of the ionization probability and is also shown in Fig. 4. For very thin foils the emission rate of electrons is constant at a value of $w=1.1\times 10^{-7}$, because ionization from ground state is dominating the electron-loss process. With increasing foil thickness other processes start contributing thereby enhanc-

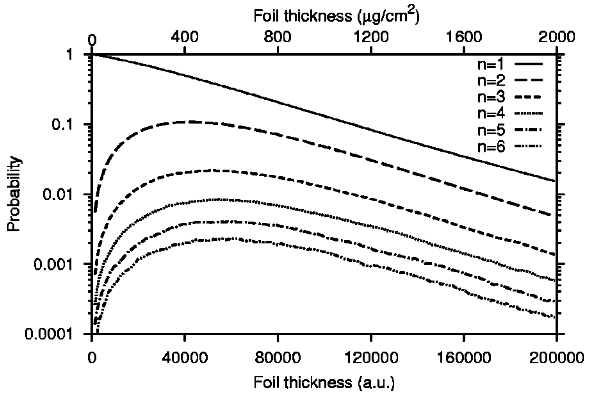

FIG. 5. Calculated populations of various n shells of Ar^{17+} as a function of propagation distance in carbon.

ing the emission rate and reaching a maximum around a propagation distance of $d=1000\ \mu\mathrm{g/cm}^2 \sim 10^5$ a.u. before rapidly decreasing.

The stepwise excitation in a random walk results in the buildup of a transient excited-state population inside the solid. Figure 5 shows the simulated evolution of the shell populations as a function of the propagation distance. Prior to transport (corresponding to the limit of thickness $d\rightarrow 0$) the electron is in the ground state ($n=1$). Since the energy gap separating it from the next excited shell is large ($\Delta E=120$ a.u.) also the required minimum momentum transfer is rather large ($q_{min}=1.3$ a.u.). Thus, mainly elastic collisions are strong enough to contribute to the excitation process of this state. Because the ground state is depopulated by a single process with a constant probability and the reverse process of increasing its population is entirely negligible, the probability for ground-state occupation obeys an exponential decay law as a function of propagation distance for small d.

Excited levels display a very different behavior. Initially, they are populated by excitation from the ground state. In the region below a foil thickness of $d<5\times 10^4$ a.u. the one-step excitation process $(n=1)\rightarrow(n>1)$ is dominant and the relative populations increase quickly by orders of magnitude. Further steps in the excitation sequence $n\rightarrow n'$ transitions becomes significant at around $d=5\times 10^4$ a.u.. For even thicker foils the processes of populating and depopulating excited states ($n>1$) equilibrate, resulting in an almost constant ratio between the populations of the various n levels (Fig. 5).

While the evolution of the excited-state populations have not been directly accessible in the present experiment, they leave a clear mark on the convoy-electron distributions. The energy and angular distributions of emitted electrons carry signatures of different pre-ionization and post-ionization processes. Detailed information about the convoy-electron emission and the postionization interactions can be obtained from the two-dimensional distribution of the parallel ($v_\parallel$) and a perpendicular ($v_\perp$) component of the velocity with respect to the beam direction (Fig. 6). For thicknesses $d \leqslant 250\ \mu\mathrm{g/cm}^2$ the distribution becomes increasingly squeezed in both $v_\parallel$ and $v_\perp$, reflecting the growth of ionization from excited states buildup in preceding collisions. This is due to the fact that electrons emitted via a stepwise excitation provide a measure of the momentum distribution (Compton profiles) immediately before ionization. As the momentum distribution of the excited states scales as Z_P/n, the velocity distribution of electrons directly ionized from such states becomes narrower for increasing n.

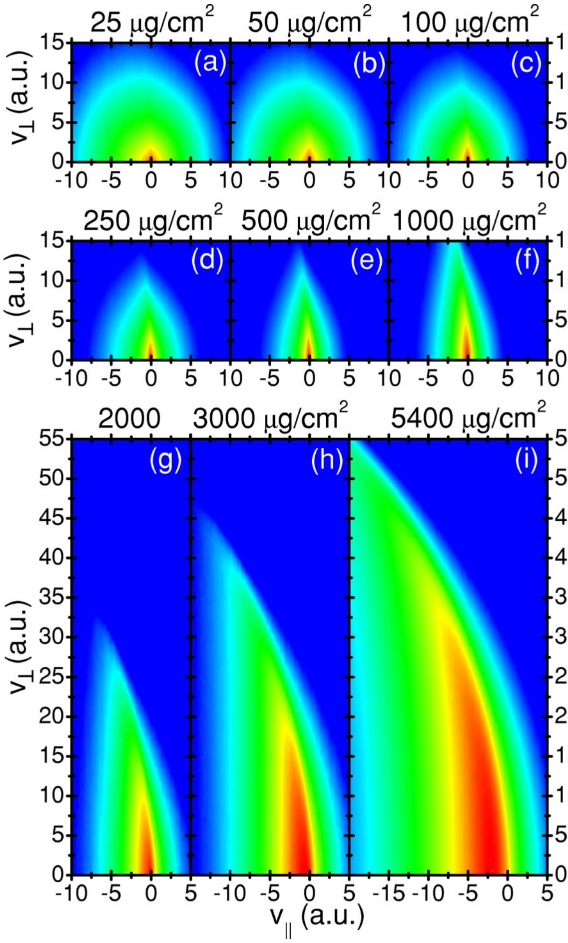

FIG. 6. (Color online) Contour plot of the velocity distribution of convoy-electrons emitted by an Ar^{17+} (390 MeV/u) traversing carbon foils of different thickness. The foil thickness is denoted in each graph and the intensities (on a logarithmic scale) have been normalized to one. We show the distribution of the parallel ($v_\parallel$) and one perpendicular ($v_\perp = v_x$ or v_y) velocity component.

Up to a foil thickness of $d=250\ \mu\mathrm{g/cm}^2$ post-ionization transport is not yet important. The velocity distribution resembles that of ion-atom collisions, more specifically, that of an ensemble of initial states with increasing weight of excited states. The distribution becomes increasingly oblate ellipsoidal [33,34] with a pronounced dominance of transverse components. During the transport through thicker foils, post-ionization collisions have a significant effect on the angular velocity distribution: broadening along a $v_\perp$ direction is the result of elastic collisions of continuum electrons whereas inelastic post-ionization collisions modify the $v_\parallel$ distribution in two ways: $v_\parallel$ is broadened and also shifted towards lower energies due to an overall energy loss (stopping) while leaving $v_\perp$ almost unaffected.

Since core collisions and electron-electron collisions have different strengths (compare momentum-transfer distribu-

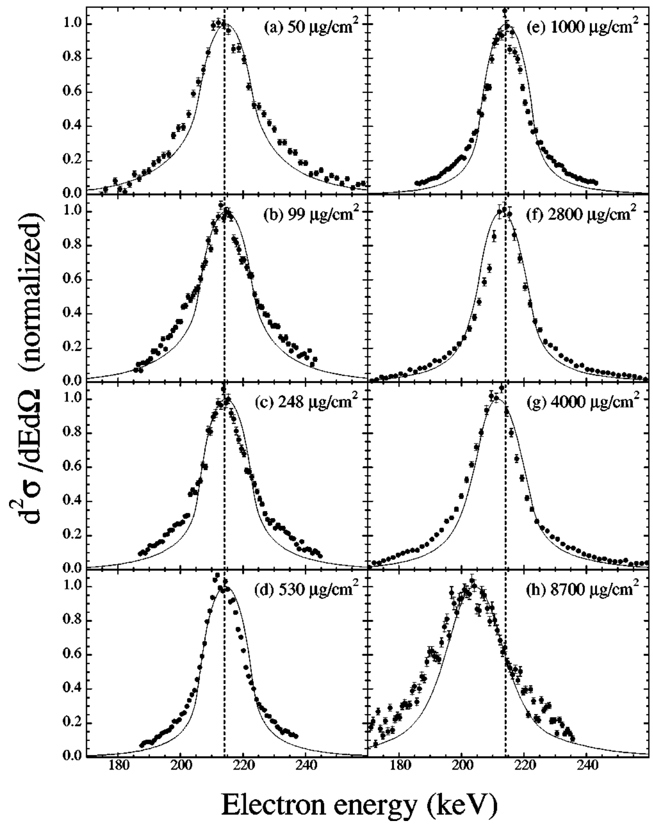

FIG. 7. Energy spectra of the electrons ejected at 0° in collisions of 390 MeV/u Ar^{17+} ions with (a) 50, (b) 99, (c) 248, (d) 530, (e) 1000, (f) 2800, (g) 4000, and (h) 8700 μg/cm^2 carbon foils. The intensities are normalized to unity at the peak positions. The vertical dashed line indicates the energy where the electron velocity equals the projectile velocity. Measurements are denoted by symbols. The solid lines show the result of the CTT simulation convoluted with the experimental resolution.

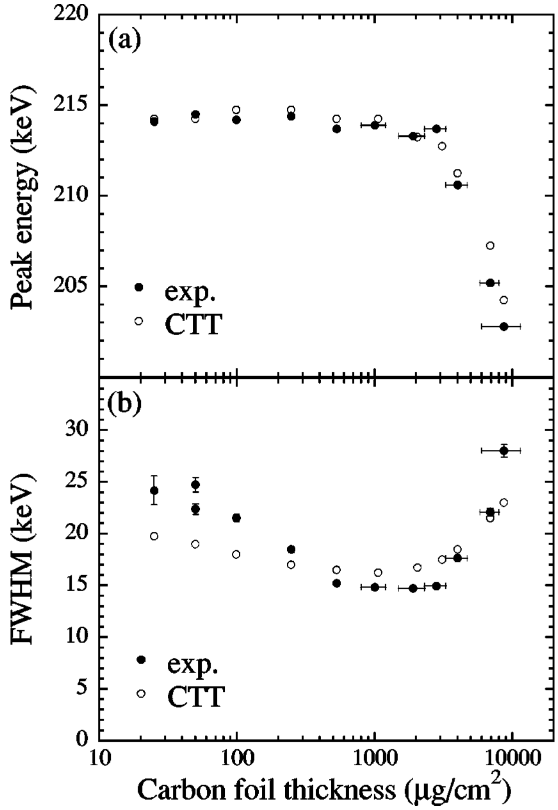

FIG. 8. (a) Peak energy and (b) width (FWHM) of the convoy-electrons as a function of carbon foil thickness for 390 MeV/u Ar^{17+} incidence. The closed and open circles show the experiment and the CTT simulation, respectively.

tions in Fig. 3), they effectively modify the continuum distribution at different propagation distances. We thus have the opportunity to disentangle the contributions of these two collisional interactions. After reaching the minimum in the perpendicular width at $d=250$ μg/cm^2, core collisions of the free electrons effectively spread the distribution along the "Newton circle"; this is spreading the angular distribution while preserving the kinetic energy. On the other hand, inelastic collisions transfer, on average, a smaller amount of momentum to the electron and broaden the $v_\parallel$ distribution noticeably after propagation through foils thicker than $d=1000$ μg/cm^2.

Figure 7 shows the experimental energy spectra of electrons ejected at 0° in collisions of 390 MeV/u Ar^{17+} ions with carbon foils. The vertical dashed line indicates the energy of the equivelocity electron (214 keV). The intensities are normalized to unity at the peak positions. The lines show the calculated spectra (see Fig. 6) convoluted with the experimental energy and angular resolution ($\Delta E=9$ keV,$\Delta\theta=1°$).

It is noted that the observed peaks are not visibly cusp shaped because the finite-energy resolution of the electron analyzer smoothes out the cusp. The energy loss of the incident ion is estimated to be 0.2 MeV/u for the thickest target (8700 μg/cm^2) leading to the energy shift of only 0.1 keV for convoy-electrons. Accordingly, the peak shift toward lower energy seen in Fig. 7, does not result from the energy loss of the ion but from the energy loss of the electron after ionization. The stopping power for 214 keV electron in carbon is 2.4 eV/(μg/cm^2) [22], and the MFP for projectile 1*s* ionization is $\sim$3000 μg/cm^2 [15], i.e., the mean energy loss of the electron for the thickest target (8700 μg/cm^2) is $\sim$16 keV in reasonable agreement with the observed energy loss. Almost all electrons ionized along the path escape the target even for thickest target since the range of 214 keV electrons in carbon is 56000 μg/cm^2 [22].

The position and width (FWHM) of the convoy spectrum as a function of target thickness are shown in Figs. 8(a) and 8(b). The CTT simulation reproduces the peak energy and peak width very well for all thicknesses. Several stages of the convoy peak evolution can be discerned.

(i) For targets thinner than 500 μg/cm^2, the peak position is at the nominal energy 214 keV isotachic to the projectile. As expected from the 2D distributions (Fig. 6) the peak widths decrease as the target thickness increases from 25 to 500 μg/cm^2.

(ii) For targets with thicknesses between 500 and 3000 μg/cm^2, the peak positions still remain at 214 keV and the peak widths remain near the minimum.

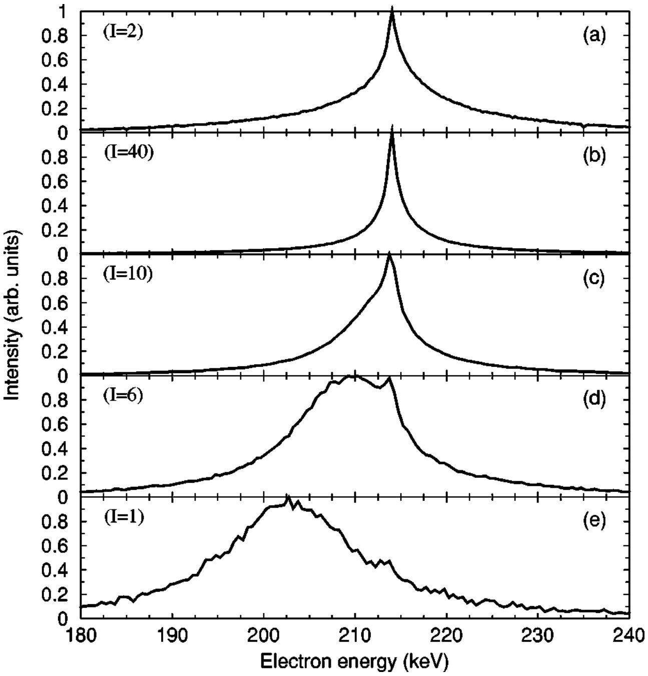

FIG. 9. Simulated convoy-electron spectra for an acceptance angle of 1° through carbon foils of a thickness of (a) $d = 50\ \mu\text{g/cm}^2$, (b) $d = 500\ \mu\text{g/cm}^2$, (c) $d = 3000\ \mu\text{g/cm}^2$, (d) $d = 5400\ \mu\text{g/cm}^2$, and (e) $d = 9000\ \mu\text{g/cm}^2$. Intensities have been normalized to unity. (Multiplication factor for intensity ratio between different thicknesses in parenthesis.)

(iii) For targets thicker than $3000\ \mu\text{g/cm}^2$, the peak is shifted to the lower-energy side and broadened with increasing target thickness. In this region of foil thicknesses, where most of the incident ions are already ionized, the post-ionization transport process, i.e., multiple collisions between liberated electrons and the target is dominant. This results in energy loss, energy straggling, and angular straggling of the electron.

In the CTT simulation two peaks appear when the energy resolution of the electron analyzer is neglected, as shown in Fig. 9. One is a cusp-shaped peak at 214 keV and the other one is a broad peak at the energy lower than 214 keV. The electrons forming the latter have suffered energy loss by multiple collisions. The double peak structure was indeed observed in the MeV/u energy region [2,18]. However, only one peak is observed in the present experiment because of the insufficient energy resolution of the electron analyzer. For thick targets, the cusp-shaped peak disappears even in the simulation neglecting the energy resolution [see Fig. 9(e)]. While the previous comparison between experiment and theory refer to normalized datasets, Fig. 10 presents the comparison between CTT and experiment for absolute yields per incident Ar^{17+} ions. These yields were obtained by integrating the singly differential spectra in the interval $E_p \pm 20$ keV (E_p is the peak energy). If all the electrons lost from the incident ions were detected, $Y(\text{Ar}^{17+})$ is proportional to the fraction of Ar^{18+} ions after passing through the carbon foil, $F_{17}(\text{Ar}^{18+})$. We evaluated the ratio of the electron yields to the charge-state fraction, $R(\text{Ar}^{17+}) = Y(\text{Ar}^{17+})/F_{17}(\text{Ar}^{18+})$ which is shown in Fig. 10(b). Indeed, $R(\text{Ar}^{17+})$ is almost constant for the targets thinner than $500\ \mu\text{g/cm}^2$. However, $R(\text{Ar}^{17+})$ decreases with increasing target thickness where the yield of the electrons detected with the analyzer with a finite acceptance angle decreases because of angular straggling.

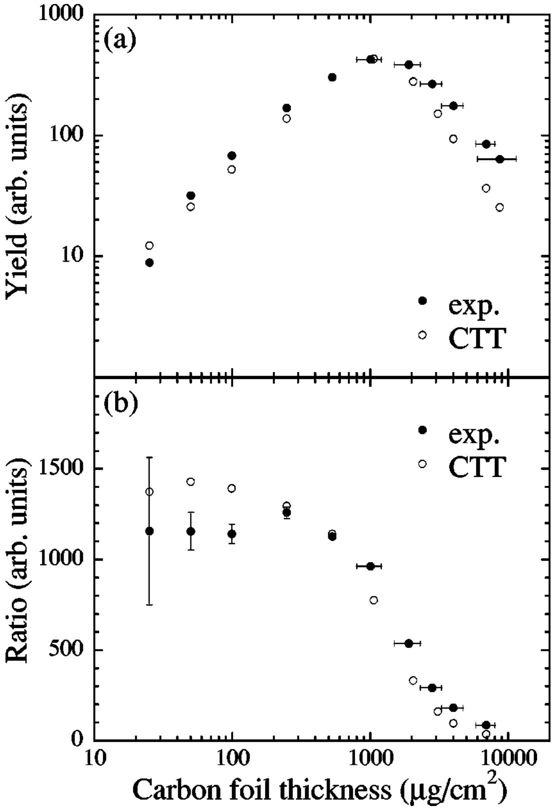

FIG. 10. (a) Yields of the convoy-electrons, $Y(\text{Ar}^{17+})$, as a function of carbon foil thickness for 390 MeV/u Ar^{17+} incidence. The simulated yields are normalized to the data at $530\ \mu\text{g/cm}^2$. (b) Ratios of the convoy-electron yields to those of the total electrons lost from the incident ions, $R(\text{Ar}^{17+}) = Y(\text{Ar}^{17+})/F_{17}(\text{Ar}^{18+})$, for 390 MeV/u Ar^{17+} ions incident on carbon foils. $F_{17}(Ar^{18+})$ represents the fraction of Ar^{18+} ions transmitted through the carbon foils for Ar^{17+} incidence. The closed and open circles show the experiment and the CTT simulation, respectively.

B. Initial-state dependence of convoy-electrons produced by 460 MeV/u Fe^{q+} ions

The experimental and theoretical results in Sec. IV A demonstrated the importance of the transient buildup of excited states for a one-electron system initially in the 1s ground state. One hallmark was the narrowing of the cusp peak until post-ionization multiple scattering sets in. Related but complementary information can be extracted by investigating the initial-state dependence. Since preparing excited initial states of a one-electron ion is experimentally not feasible in view of the extremely short lifetimes, the initial-state dependence can, instead, be explored by using multielectron projectiles. In view of the sequential nature of the stripping process ordered according to the binding energy as discussed in Sec. III, the initial-state dependence can be investigated. As test case we employ hydrogenic [$\text{Fe}^{25+}(1s)$], helium-

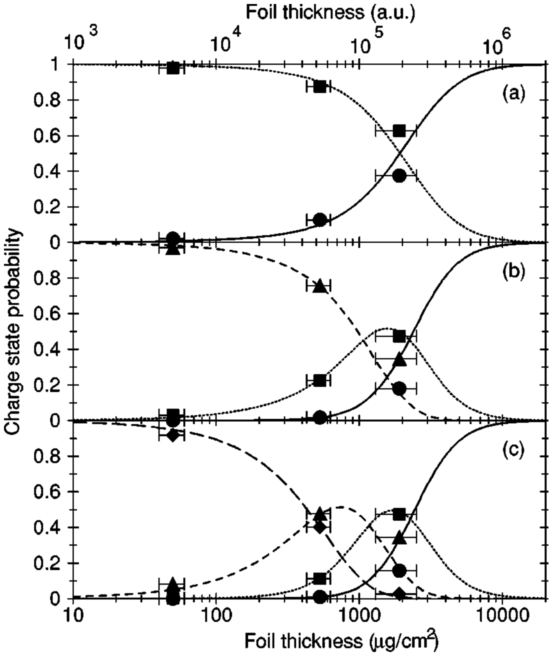

FIG. 11. Charge state fractions as a function of foil thickness for different incident projectiles: (a) Fe^{25+}, (b) Fe^{24+}, and (c) Fe^{23+} with an energy of 460 MeV/u. Lines represent the CTT simulation: full line, Fe^{26+}; dotted, Fe^{25+}; dashed, Fe^{24+}; and long dashed, Fe^{23+}. Symbols represent the experimental data: circle, Fe^{26+}; square, Fe^{25+}; triangle, Fe^{24+}; and diamond, Fe^{23+}.

like $[Fe^{24+}(1s^2)]$, and lithiumlike $[Fe^{23+}(1s^2,2s)]$ ions. Figure 11 shows the evolution of the charge-state distribution of 460 MeV/u Fe^{q+} for $q=25,24$, and 23 incident on a carbon foil as a function of the thickness. The CTT simulation employing the IPA discussed in Sec. III is in good agreement with the data. It should be noted that no empirical charge-changing cross section, as frequently used in rate-equation approaches, enters the simulation but the charge-state and continuum spectrum is calculated self-consistently from the microscopic Langevin equation (Eq. 1).

Spectra of emitted electrons ejected near 0° were measured for thicknesses ranging from 50 to 1900 μg/cm^2 (Fig. 12). Overall, good agreement with the CTT can be found for all incident charge states and all thicknesses. More detailed information can be extracted from the yield and the width (FWHM) of the convoy peak (Fig. 13). The yield [Fig. 13(a)] clearly indicates the sequential nature of the stripping process. Initially, the loss process is fastest for the relatively loosely bound 2*s* electron followed by the heliumlike 1s electron (already a factor $\simeq 6$ smaller) while the hydrogenic 1*s* electron produces a yield initially somewhat below the statistical ratio (1:2) relative to the heliumlike configuration. For thick foils we observe the approach to a statistical yield distribution (1:2:3) for hydrogen-, helium-, and lithium-like ions when all electrons had sufficient time to complete their random walk to the continuum irrespective of their initial state.

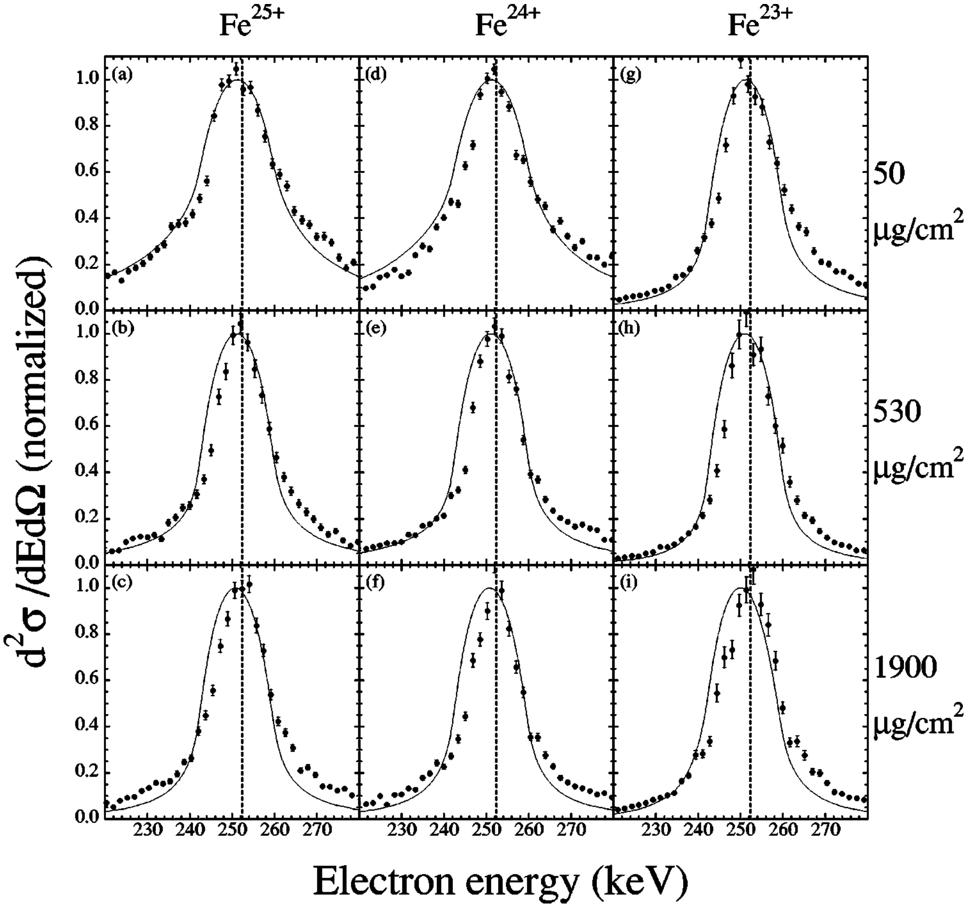

FIG. 12. Energy spectra of electrons ejected at 0° in collisions of 460 MeV/u $Fe^{25+,24+,23+}$ ions with 50, 530, and 1900 μg/cm^2 carbon foils. The solid lines show the result of the CTT simulation.

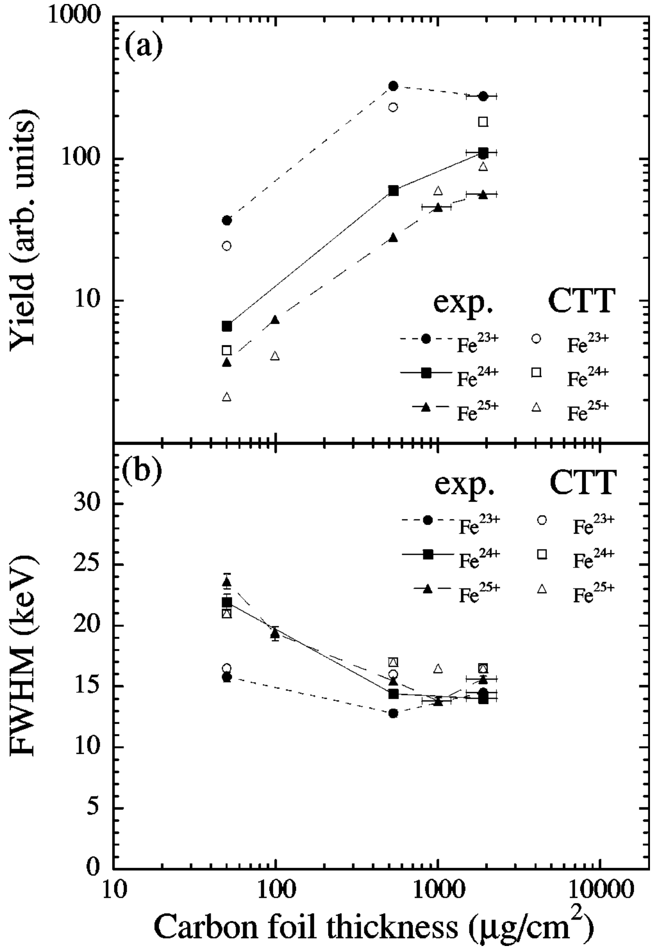

FIG. 13. (a) Yields of the detected electrons, $Y(\mathrm{Fe}^{q+})$, as a function of carbon foil thickness for 460 MeV/u incident Fe^{25+}, Fe^{24+}, and Fe^{23+}, respectively. The simulated yields are normalized at 530 μg/cm^2 for Fe^{25+} incidence. (b) Width (FWHM) of the convoy-electrons as a function of carbon foil thickness for 460 MeV/u incident Fe^{q+}. The closed and open symbols show the experiment and simulation, respectively.

The cusp width [Fig. 13(b)] provides evidence for the role of higher *n* shells in narrowing the cusp, either being initially available or being later dynamically produced during the evolution inside the solid. For Li-like Fe^{23+} ions incident on thin targets (50 μg/cm^2 carbon foil), the width of the convoy-electron peak is significantly narrower than those for Fe^{25+} and Fe^{24+}. In the single-collision regime the contribution of the initially more loosely bound $2s$ electron to the convoy-electron production is dominant. As mentioned above, the peak width of ELC cusp for higher-lying states (the $2s$ electron) is narrower than for $1s$ electrons reflecting the momentum distribution, i.e., the Compton profile of the initial state of the emitted electron [10]. The observed result directly confirms this prediction for the initial-state dependence disentangled from the evolution of the excited-state distribution. By contrast, for thicker foils the convoy peak narrows for hydrogenic and helium-like projectiles dramatically and approaches that of the Li-like projectiles since now $2s$ and higher lying states are populated by sequential excitation inside the foil.

In the MeV/u energy region, the convoy-electron spectra reflecting the initial state of the electron in the projectile could not be unambiguously detected because single-collision conditions are difficult to fulfill. We note however that Moshammer *et al.* [35] have recently measured the spectra of the low-energy electrons ejected from a target atom in gas phase in ion-atom collisions of 3.6 MeV/u Au^{53+} ions with Ne and Ar atoms and observed a structure in the electron spectrum dependent on the initial state in the target atom. These electrons in the target frame resemble convoy-electrons in the projectile frame (reversed kinematics) except that the former is emitted from a neutral atom by ion impact. In either case, electrons are produced in the soft collisions where the transverse momentum transfer plays a more important role than the longitudinal momentum transfer, i.e., parallel to the beam direction. Thus, the momentum distribution of the initial state is projected onto that of the continuum state providing complementary information on the initial-state dependence in the single-collision regime.

V. SUMMARY

We have presented a joint experimental and theoretical study of the charge-state evolution and energy spectra of electrons ejected in forward direction in collisions of 390 MeV/u Ar^{17+} and 460 MeV/u $\mathrm{Fe}^{25+,24+,23+}$ ions with carbon foils of various thicknesses. Because of the high charge, high projectile energies, and a wide range of thicknesses the path of sequential excitation and ionization of an initially bound electron could be followed—for ion-solid collisions—in unprecedented detail. The buildup of excited states is, through the narrowing of the Compton profile, clearly reflected in the narrowing of the convoy peak. The width of the convoy peak evolves nonmonotonically as a function of the foil thickness: narrowing due to the generation of projectile excitation by multiple scattering is followed by broadening in both energy and angle due to further multiple scattering of the liberated electrons. The charge-state distributions of the transmitted ions and the convoy-electron spectra calculated by the CTT simulation are in a good agreement with the experiment over a wide range of target thicknesses, i.e., from a single-collision regime to a multiple-collision regime lending support to this scenario. Apart from corrections for the minimum momentum transfer for deeply bound states, the simulation proceeds within the framework of classical dynamics. As quantum effects have recently been analyzed for x-ray emission [8,9], their presence in the convoy-electron spectrum remains an open question.

ACKNOWLEDGMENTS

We thank Dr. K. Shima for the measurement of the carbon foil thicknesses at the University of Tsukuba. The experimental work was supported in part by Matsuo Foundation, the Sumitomo Foundation, the Mitsubishi Foundation, and a Grant-in-Aid for Scientific Research (Grant No. 13440126) from the Japan Society for the Promotion of Science. This experiment is one of the research projects with heavy ions atNIRS-HIMAC. The theoretical part was supported by the Austrian FWF. C.O.R. acknowledges support by the DCS, OBES, U.S. DOE, through ORNL managed by UT-Battelle, LLC, under Contract No. DE-AC05-00OR22725. K.T. gratefully acknowledges the support from the Hungarian Scientific Research Fund: OTKA Grant No. T032306 and the grant ‘‘Bolyai’’ from the Hungarian Academy of Sciences and TéT Grant No. A-19/2001.

[1] M. Breinig, S.B. Elston, S. Huldt, L. Liljeby, C.R. Vane, S.D. Berry, G.A. Glass, M. Schauer, I.A. Sellin, G.D. Alton, S. Datz, S. Overbury, R. Laubert, and M. Suter, Phys. Rev. A **25**, 3015 (1982).
[2] Y. Yamazaki and N. Oda, Phys. Rev. Lett. **52**, 29 (1984).
[3] F. Drepper and J. Briggs, J. Phys. B **9**, 2063 (1976).
[4] S.D. Berry, G.A. Glass, I.A. Sellin, K.-O. Groeneveld, D. Hofmann, L.H. Andersen, M. Breinig, S.B. Elston, P. Engar, M.M. Schauer, N. Stolterfoht, H. Schmidt-Böcking, G. Nolte, and G. Schiwietz, Phys. Rev. A **31**, 1392 (1985).
[5] R. Shakeshaft and L. Spruch, Rev. Mod. Phys. **51**, 369 (1979).
[6] J. Macek, Phys. Rev. A **1**, 235 (1970).
[7] M.S. Gulley, P.B. Keating, H.C. Bryant, E.P. MacKerrow, W.A. Miller, D.C. Rislove, S. Cohen, J.B. Donahue, D.H. Fitzgerald, S.C. Frankle, D.J. Funk, R.L. Hutson, R.J. Macek, M.A. Plum, N.G. Stanciu, O.B. van Dyck, C.A. Wilkinson, and C.W. Planner, Phys. Rev. A **53**, 3201 (1996).
[8] J.P. Rozet, D. Vernhet, I. Bailly-Despiney, C. Fourment, and L.J. Dubé, J. Phys. B **32**, 4677 (1999).
[9] D. Vernhet, J.P. Rozet, E. Lamour, B. Gervais, C. Fourment, and L.J. Dubé, Phys. Scr. **T80A**, 83 (1999).
[10] J. Burgdörfer, M. Breinig, S.B. Elston, and I.A. Sellin, Phys. Rev. A **28**, 3277 (1983).
[11] S.B. Elston, S.D. Berry, J. Burgdörfer, I.A. Sellin, M. Breinig, R. DeSerio, C.E. Gonzalez-Lepera, L. Liljeby, K.-O. Groeneveld, D. Hofmann, P. Koschar, and I.B.E. Nemirovsky, Phys. Rev. Lett. **55**, 2281 (1985).
[12] S.D. Berry, S.B. Elston, I.A. Sellin, M. Breinig, R. DeSerio, C.E. Gonzalez-Lepera, and L. Liljeby, J. Phys. B **19**, L149 (1986).
[13] J.P. Gibbons, S.B. Elston, K. Kimura, R. DeSerio, I.A. Sellin, J. Burgdörfer, J.P. Grandin, A. Cassimi, X. Husson, L. Liljeby, and M. Druetta, Phys. Rev. Lett. **67**, 481 (1991).
[14] Y. Takabayashi, T. Ito, T. Azuma, K. Komaki, Y. Yamazaki, H. Tawara, M. Torikoshi, A. Kitagawa, E. Takada, and T. Murakami, Phys. Scr. **T80B**, 249 (1999).
[15] J.P. Rozet, C. Stéphan, and D. Vernhet, Nucl. Instrum. Methods Phys. Res. B **107**, 67 (1996).
[16] P. Kürpick, C.O. Reinhold, J. Burgdörfer, and B. Gervais, Phys. Rev. A **58**, 2183 (1998).
[17] J. Burgdörfer and J. Gibbons, Phys. Rev. A **42**, 1206 (1990).
[18] C.O. Reinhold, J. Burgdörfer, J. Kemmler, and P. Koschar, Phys. Rev. A **45**, R2655 (1992).
[19] T. Minami, C.O. Reinhold, M. Seliger, J. Burgdörfer, C. Fourment, E. Lamour, J.P. Rozet, D. Vernhet, and B. Gervais, Phys. Rev. A **65**, 032901 (2002).
[20] T. Minami, C.O. Reinhold, and J. Burgdörfer, Phys. Rev. A **67**, 022902 (2003).
[21] J. McGuire, *Electron Correlation Dynamics in Atomic Collisions* (Cambridge University Press, Cambridge, 1997).
[22] L. Pages, E. Bertel, H. Joffre, and L. Sklavenitis, At. Data **4**, 1 (1972).
[23] The values of the accuracy and inhomogeneity of the carbon foil thickness are provided by a carbon foil supplier (Arizona Carbon Foil Co.).
[24] M. Seliger *et al.* (unpublished).
[25] B. Gervais, C.O. Reinhold, and J. Burgdörfer, Phys. Rev. A **53**, 3189 (1996).
[26] J. D. Jackson, *Classical Electrodynamics* (Wiley, New York, 1999).
[27] J. Burgdörfer, *The Physics of Electronic and Atomic Collisions*, edited by A. Dalgarno, R. Freund, P. Koch, M. Lubell, and T. Lucatorto, AIP Conf. Proc. No. 205 (AIP, New York, 1990), p. 476.
[28] L. I. Schiff, *Quantum Mechanics* (McGraw-Hill, New York, 1955).
[29] U. Fano, Annu. Rev. Nucl. Sci. **13**, 1 (1963).
[30] C. Ashley, J.J. Cowan, R.H. Ritchie, V.E. Anderson, and J. Hoelzl, Thin Solid Films **60**, 361 (1979).
[31] M.W. Williams and E.T. Arakawa, J. Appl. Phys. **43**, 3460 (1972).
[32] B. H. Bransden and C. J. Joachain, *Physics of Atoms and Molecules* (Longman, London, 1983).
[33] M. Seliger, K. Tőkési, C.O. Reinhold, and J. Burgdörfer, Nucl. Instrum. Methods Phys. Res. B **205**, 830 (2003).
[34] G. Szabó, J. Wang, and J. Burgdörfer, Phys. Rev. A **48**, R3414 (1993).
[35] R. Moshammer, P.D. Fainstein, M. Schulz, W. Schmitt, H. Kollmus, R. Mann, S. Hagmann, and J. Ullrich, Phys. Rev. Lett. **83**, 4721 (1999).